Engineering Structures 294 (2023) 116724

Contents lists available at ScienceDirect

Engineering Structures

journal homepage: www.elsevier.com/locate/engstruct

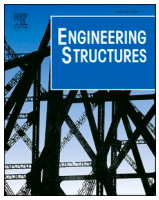

Robust numerical solution for assessing corrosion of reinforced concrete structures under external power supply

Bin Dong [a], Yuguo Yu [b,*], Yuan Feng [a], Di Wu [c], Gaofeng Zhao [d], Airong Liu [b], Wei Gao [a,*]

[a] Centre for Infrastructure Engineering and Safety, School of Civil and Environmental Engineering, The University of New South Wales, Sydney, NSW 2052, Australia
[b] Research Center for Wind Engineering and Engineering Vibration, Guangzhou University, Guangzhou 510006, China
[c] Centre for Built Infrastructure Research (CBIR), School of Civil and Environmental Engineering, University of Technology Sydney, Sydney, NSW 2007, Australia
[d] State Key Laboratory of Hydraulic Engineering Simulation and Safety, School of Civil Engineering, Tianjin University, Tianjin 300354, China

ARTICLE INFO

Keywords:
Accelerated corrosion
Cathodic protection
Finite element method
Power supply
Reinforced concrete structures

ABSTRACT

Impressing current is a popular technique to adjust corrosion behaviors of structures, both in academic investigation and engineering practice. Focusing on the specific problem, this paper presents a robust solution strategy for analyzing corrosion of reinforced concrete structures, under both voltage-controlled and current-controlled power supply. Following fundamental electrochemistry, a nonlinear numerical model incorporating field and global variables is developed, where the ways of considering power supplies with different controlling modes are presented. To tackle the essential global variable to problems under current-controlled power supply, a pseudo discretization method is newly developed to facilitate the highly nonlinear finite element analysis. Given moisture-induced nonuniform concrete resistivity, the moisture field in concrete is also modelled and solved together with the corrosion propagation through a staggered solution scheme. The proposed approach is carefully validated against a variety of reported experiments. Moreover, by directly controlling steel passivation state, the influence of steel depassivation extent on the cathodic protection performance for aging reinforced concrete structures under different saturation degree is numerically investigated for the first time. It is discovered that the protection effectiveness is closely related to the steel depassivation state. It is also revealed that the influence of concrete saturation degree on protection performance in a current-controlled system is generally more complex than that of a voltage-controlled system.

1. Introduction

Detrimental impacts of corrosion on reinforced concrete infrastructures, such as cross-sectional loss of reinforcements and cracking of the cover concrete, have long been recognized [1–6]. The cost for annual restoration of corroded structures brings considerable financial burden to many countries [7]. In general, it is well established that steel corrosion in concrete is an electrochemical process and inevitably affected by electric interferences [8]. For various purposes, external power supply is widely imposed on the electrochemical system by academics and engineers to adjust steel corrosion behavior.

Given that natural steel corrosion is a long-term process, numerous researchers have successfully improved the efficiency of experimental studies by impressing current [9–16], see Fig. 1 (a). Under this circumstance, an enforced macrocell corrosion occurs, with the steel as anode and an auxiliary electrode as cathode, where electrons from the power supply are consumed by the reduction reaction on the cathode. As a result, an equal number of electrons should be supplied by the iron dissolution reaction, hence accelerating corrosion rate. On the other hand, suppressing corrosion of reinforced concrete structures by external power sources is also common in engineering practices [17–24], namely impressed current cathodic protection (ICCP) as shown in Fig. 1 (b). In ICCP, electrons flow towards protected steel reinforcement to produce cathodic polarization. Previous studies have demonstrated that the method could ease the corrosion process to achieve longer service life for aging structures [25].

Despite the extensive practical applications, only limited and incomplete numerical analyses on the power supply-involved corrosion system have been reported [26–30], which is mainly caused by the lack of robust solution method for solving the highly nonlinear problem. In general, the nonlinearity source for electrochemistry-based corrosion analyses lies in the boundary condition associated with the electrode

* Corresponding authors.
E-mail addresses: yuguo.yu@gzhu.edu.cn (Y. Yu), w.gao@unsw.edu.au (W. Gao).

https://doi.org/10.1016/j.engstruct.2023.116724
Received 31 March 2023; Received in revised form 29 June 2023; Accepted 31 July 2023
Available online 9 August 2023

polarization [31]. With the further consideration of impressed current, the nonlinearity of the resulted numerical system is enhanced, depending on the detailed technique for power supply. To be specific, the nonlinearity is intensified in the current-controlled mode due to the unknown applied voltage, where an extra nonlinear governing equation needs to be introduced to solve the complex mixed field and global variables. Except for these intrinsic nonlinearities, coupling with other fields in concrete, such as moisture field, further complicates the overall corrosion modelling [32].

To fill the research gap, this paper presents a robust solution strategy to tackle the complex numerical system. Following the electrochemical theory, the corrosion propagation of reinforced concrete structures under both voltage-controlled and current-controlled power supply is modelled and solved via finite element method. Especially, a pseudo discretization method is freshly proposed to handle the global variable, i.e., applied voltage, in the highly nonlinear analysis on problems under current-controlled power supply. In view of time-dependent and nonuniform concrete resistivity induced by the variation in saturation degree, the moisture transport in concrete is also investigated. The proposed method is realized through an in-house code in MATLAB and validated against reported accelerated corrosion experiments. Furthermore, the developed method is also employed to investigate the cathodic protection for aging reinforced concrete structures, where localized reinforcement corrosion proceeds with chloride ingress [33]. In engineering practice, chloride-induced depassivation state of reinforcement is uncertain when anti-corrosion measure is implemented, which affects the protection performance and has yet been thoroughly investigated so far. Based on the proposed method, the detailed passivation status of rebars can be handled in a straightforward manner, where the influence of existing steel depassivation area on corrosion mitigation of reinforced concrete structures under different saturation states is systematically assessed for the first time.

2. Model formulation

2.1. Electrode polarization

According to electrochemical fundamentals [34], kinetics of electrode reactions are governed by the electrode polarization, which can be represented mathematically by Tafel's equation. In the power supply-involved corrosion process, electrode reactions depend on the detailed method for connecting the electrochemical system with the external power source. For general purposes, we define the rate of various oxidation and reduction reactions on anode and cathode in Eqs. (1)–(2).

$$i_{\mathrm{a},j} = (-1)^{\vartheta} i^{0}_{\mathrm{a},j} \exp\left[\frac{2.303(V_{\mathrm{a}} - \varphi - E_{\mathrm{a},j})}{\beta_{\mathrm{a},j}}\right] \tag{1}$$

$$i_{\mathrm{c},k} = (-1)^{\vartheta} i^{0}_{\mathrm{c},k} \exp\left[\frac{2.303(V_{\mathrm{c}} - \varphi - E_{\mathrm{c},k})}{\beta_{\mathrm{c},k}}\right] \tag{2}$$

where subscript a, j means the jth reaction on anode, subscript c, k means the kth reaction on cathode, $\vartheta = 0$ and 1 for the oxidation and reduction reaction, respectively. Following the conventions, i is the current density (A/m^2), i^0 is the exchange current density (A/m^2), V is the electric potential of electrodes (V), φ is the electric potential of concrete (V), E is the equilibrium potential (V vs. SCE) and β is the Tafel's slope (V/dec).

Despite that rates of most electrode reactions obey aforementioned equations, the oxygen reduction reaction in the steel corrosion process is further constrained by the oxygen accessibility [35], i.e., concentration polarization. In this regard, Tafel's equation with a limiting current density is applied to this specific reaction [1,8], see Eqs. (3)–(4).

$$i_{\mathrm{O_2}} = -\frac{i^{0}_{\mathrm{O_2}} \cdot \exp\left(\frac{2.303(V_{\mathrm{a/c}} - \varphi - E_{\mathrm{O_2}})}{\beta_{\mathrm{O_2}}}\right)}{1 + \frac{i^{0}_{\mathrm{O_2}}}{i_{\mathrm{L}}} \cdot \exp\left(\frac{2.303(V_{\mathrm{a/c}} - \varphi - E_{\mathrm{O_2}})}{\beta_{\mathrm{O_2}}}\right)} \tag{3a}$$

$$i_{\mathrm{L}} = \frac{D_{\mathrm{O_2}} z_{\mathrm{O_2}} \mathrm{F} c^{\mathrm{ext}}_{\mathrm{O_2}}}{L} \tag{3b}$$

$$D_{\mathrm{O_2}} = 1.92 \times 10^{-6} \times \left(\frac{\phi}{1-\chi}\right)^{1.8} \cdot [1 - \theta(RH)]^{2.2} \tag{4}$$

where in Eq. (3), subscript a/c indicates that the reaction could happen on either anode or cathode, subscript $\mathrm{O_2}$ denotes the oxygen reduction reaction, i_{L} is the limiting current density (A/m^2) controlled by oxygen availability, $D_{\mathrm{O_2}}$ is the oxygen diffusivity (m^2/s), $z_{\mathrm{O_2}} = 4$ is the valency (-) of oxygen reduction reaction, F is the Faraday constant (96485.333 C/mol), L is the shortest length (m) from the electrode surface to the exposure surface, $c^{\mathrm{ext}}_{\mathrm{O_2}}$ is the oxygen concentration (mol/m^3) in the exposure environment. In Eq. (4), ϕ is concrete porosity (-), χ is volume fraction (-) of aggregates in the concrete mix, θ is the concrete saturation ratio (-) as a function of relative humidity (RH).

2.2. Electric field in concrete

As shown in Tafel's equations, the electric field in concrete plays a central role in evaluating the electrochemical reaction rate. In this study, the potential distribution in concrete is modelled by the classical Laplace's equation [36–38], as shown in Eq. (5). The electrode polarization-related boundary conditions, as written in Eqs. (6)–(7), give rise to the high nonlinearity of the overall numerical system.

$$\nabla \cdot \boldsymbol{i} = 0 \tag{5a}$$

$$\boldsymbol{i} = -\frac{1}{\rho}\nabla\varphi \tag{5b}$$

$$-\boldsymbol{i}\cdot\boldsymbol{n}|_{\Gamma_{\mathrm{a}}} = i_{\mathrm{a}} = \sum_{j} i_{\mathrm{a},j} \tag{6}$$

$$-\boldsymbol{i}\cdot\boldsymbol{n}|_{\Gamma_{\mathrm{c}}} = i_{\mathrm{c}} = \sum_{k} i_{\mathrm{c},k} \tag{7}$$

where in Eq. (5), $\boldsymbol{i}$ is the current density vector in concrete (A/m^2), ρ is the electrical resistivity of concrete (Ω·m). In Eqs. (6)–(7), $\boldsymbol{n}$ is the unit

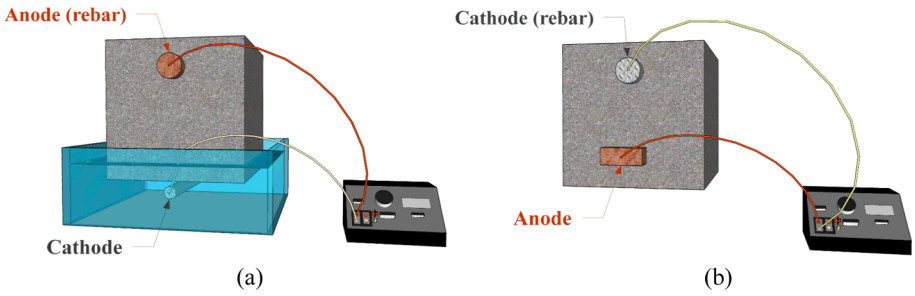

Fig. 1. Schematic diagram of: (a) accelerated corrosion experiment; (b) ICCP of reinforced concrete.

normal vector pointing outward from the electrode surface, Γ_a and Γ_c are the surface of anode and cathode, respectively, i_a and i_c are net current density (A/m^2) on surface of anode and cathode, respectively.

Concrete resistivity, essential to the Laplace's model, strongly relies on the material saturation degree according to the previous study [39]. To this end, an empirical equation reported by Garcia et al. [40] is employed to take the effect into account, see Eq. (8), where the moisture field is evaluated by the Richard's equation [41], as written in Eqs. (9)–(11).

$$\rho = 0.437 w_L^{-2.53} = 0.437[\phi \cdot \theta(RH)]^{-2.53} \tag{8}$$

$$\Psi \frac{\partial RH}{\partial t} - \nabla \cdot (D_M \nabla RH) = 0 \tag{9a}$$

$$D_M = \frac{\rho_L D_L + \rho_{VS} D_V}{\rho_L} \tag{9b}$$

$$\Psi = \phi \frac{\partial \theta(RH)}{\partial RH} \tag{9c}$$

$$D_L = \frac{K}{\mu} w_L \overline{P}_{CS} \tag{10}$$

$$D_V = w_G D / \tau \tag{11}$$

where in Eq. (8), w_L is the volume fraction of liquid water in concrete (-). In Eqs. (9)–(11), D_M is the overall moisture diffusivity (m^2/s), D_L and ρ_L are the diffusivity (m^2/s) and density (kg/m^3) of liquid water, D_V and ρ_{VS} are the diffusivity (m^2/s) of vapor water and saturated vapor density (kg/m^3), K is the permeability of concrete with the consideration of the pore structure (m^2), μ is the viscosity of the pore solution (-), $\overline{P}_{CS}$ is the average saturation vapor pressure (Pa), w_G is the volumetric content of vapor (m^3/m^3), D is the intrinsic diffusivity of vapor water (m^2/s), and τ is the concrete tortuosity (-), where the detailed evaluation approach refers to [41].

2.3. External power supply

The other key to evaluating kinetics of electrode reactions is the correct representation of electrode potentials, which are often regarded as 0 in the modelling of natural corrosion. In the present electrochemical system, however, the corresponding values depend on the power source. Assuming that the resistivity of electrodes and power supply wires are negligible relative to that of the concrete, potentials of electrodes distribute uniformly and correspond to the applied voltage (V_{app}). As a result, the consideration of the voltage-controlled power supply in the electrochemical model is in a straightforward manner, as shown in Eqs. (12)–(13).

$$V_c = 0 \tag{12}$$

$$V_a = V_{app} \tag{13}$$

Nevertheless, regarding the current-controlled power supply, V_{app} becomes a variable to maintain the average net current density on anode, namely applied current density (i_{app}). As a result, the changing voltage cannot be directly applied in Tafel's equations for evaluating anodic polarization. In this specific case, this crucial parameter indeed is governed by Eq. (14), where the analysis is further complicated by not only the increased model nonlinearity but also the involvement of an extra variable, i.e., V_{app}. To handle this special variable, a pseudo discretization method is proposed in the solution scheme, which will be discussed in detail in Section 3.

$$\begin{aligned} \int_{\Gamma_a} i_a \mathrm{d}s &= \int_{\Gamma_a} \sum_j (-1)^{\vartheta} i_{a,j}^0 \exp\left[\frac{2.303\left(V_{app} - \varphi - E_{a,j}\right)}{\beta_{a,j}}\right] \mathrm{d}s \\ &= \int_{\Gamma_a} i_{app} \, \mathrm{d}s \end{aligned} \tag{14}$$

3. Solution strategy

3.1. Solution procedures

To solve the complex numerical problem of reinforcement corrosion under external power supply, a numerical procedure is developed herein. The simultaneous moisture transportation and electrochemical corrosion analysis are decoupled by a staggered solution scheme, as illustrated in Fig. 2. After the determination of RH field in the staggered step 1, the electrochemical analysis is conducted in the staggered step 2 based on the RH-controlled concrete resistivity and oxygen accessibility.

3.2. Finite element formulation

To successfully implement the proposed numerical procedure, detailed algorithms for solving both stagger steps are developed based on finite element method. Herein, particular emphasis is put on the solution process of current-controlled analysis, in which a pseudo discretization method is proposed.

3.2.1. Moisture transportation

According to finite element theory [42], the weak form for the moisture transportation analysis is first established in Eq. (15), which is further discretized spatially by the Galerkin method, see Eqs. (16)–(20).

$$\int_\Omega W_{RH} \Psi \dot{RH} + \nabla W_{RH} \cdot D_M \nabla RH \, \mathrm{d}\Omega = 0 \tag{15}$$

$$\boldsymbol{M}_{RH} \dot{\boldsymbol{U}}_{RH} + \boldsymbol{K}_{RH} \boldsymbol{U}_{RH} = \boldsymbol{F}_{RH} \tag{16}$$

with

$$\dot{\boldsymbol{U}}_{RH} = \begin{bmatrix} \dot{RH}_1 & \cdots & \dot{RH}_{nn-1} & \dot{RH}_{nn} \end{bmatrix}^T \tag{17}$$

$$\boldsymbol{U}_{RH} = \begin{bmatrix} RH_1 & \cdots & RH_{nn-1} & RH_{nn} \end{bmatrix}^T \tag{18}$$

$$\boldsymbol{M}_{RH} = \int_\Omega \boldsymbol{N}^T \Psi \boldsymbol{N} \, \mathrm{d}\Omega \tag{19}$$

$$\boldsymbol{K}_{RH} = \int_\Omega \boldsymbol{B}^T \boldsymbol{D}_{RH} \boldsymbol{B} \, \mathrm{d}\Omega \tag{20}$$

where W_{RH} is the weighting function of RH, $\dot{RH}$ is the time derivative of RH, Ω denotes the domain of one finite element, $\boldsymbol{M}_{RH}$, $\boldsymbol{K}_{RH}$ and $\boldsymbol{F}_{RH}$ are damping matrix, stiffness matrix and force vector for RH analysis, respectively, note that $\boldsymbol{F}_{RH}$ results from Dirichlet boundary conditions, $\boldsymbol{U}_{RH}$ and $\dot{\boldsymbol{U}}_{RH}$ are vectors that consist of nodal RH and time derivatives of them, nn is the number of nodes in one finite element, $\boldsymbol{N}$ is the vector containing shape functions, $\boldsymbol{B}$ is the matrix formed by spatial derivatives of shape functions, and $\boldsymbol{D}_{RH} = \mathrm{diag}(D_M, D_M)$ is the moisture diffusivity matrix.

Moreover, to deal with the time derivative terms in Eq. (16), we apply the implicit Euler method for the temporal discretization in the time-dependent analysis, yielding a system of equations as shown in Eqs. (21)–(23).

$$\widetilde{\boldsymbol{K}}_{RH} \boldsymbol{U}_{RH} - \widetilde{\boldsymbol{F}}_{RH} = \boldsymbol{0} \tag{21}$$

with

$$\widetilde{\boldsymbol{K}}_{RH} = \boldsymbol{M}_{RH} + \Delta t \boldsymbol{K}_{RH} \tag{22}$$

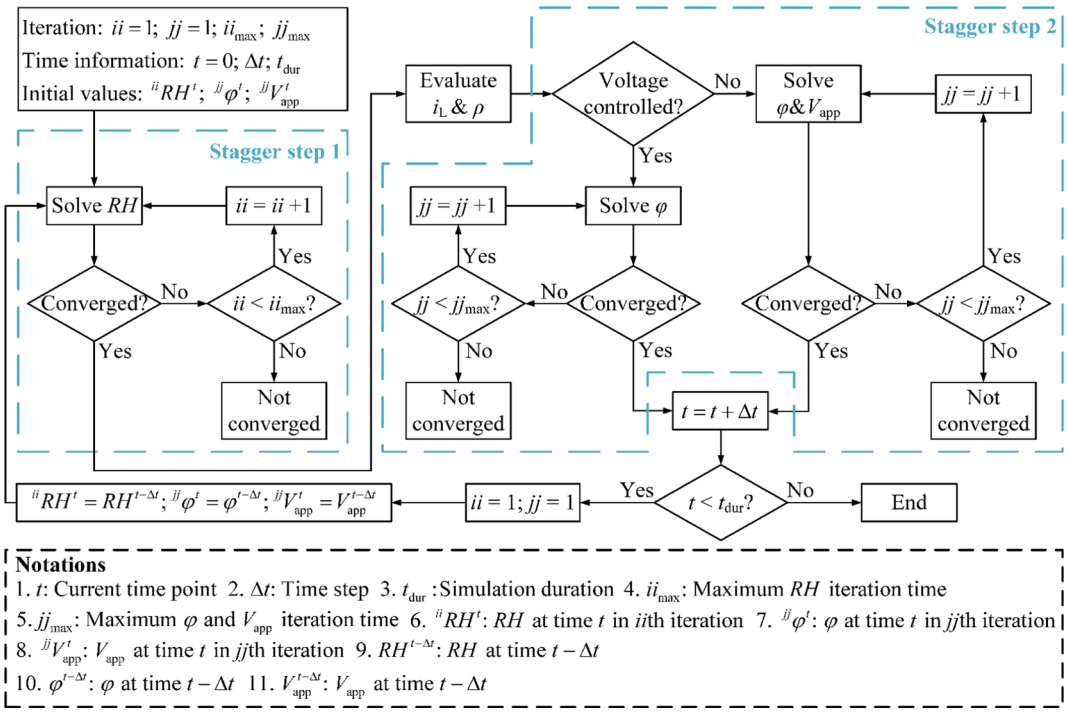

Fig. 2. Numerical procedure for reinforcement corrosion analysis under external power supply.

$$\widetilde{\boldsymbol{F}}_{\mathrm{RH}} = \boldsymbol{M}_{\mathrm{RH}}\overleftarrow{\boldsymbol{U}}_{\mathrm{RH}} + \Delta t\boldsymbol{F}_{\mathrm{RH}} \tag{23}$$

where $\widetilde{\boldsymbol{K}}_{\mathrm{RH}}$ and $\widetilde{\boldsymbol{F}}_{\mathrm{RH}}$ are modified stiffness matrix and force vector after the application of implicit Euler method, $\overleftarrow{\boldsymbol{U}}_{\mathrm{RH}}$ is the vector consisting of nodal RH of last time step, Δt is the time step of analysis.

3.2.2. Electrochemical analysis

As demonstrated in Section 2, depending on the detailed technique for controlling power supply, different electrochemical models are defined. In the voltage-controlled analysis, only a field variable is involved, i.e., φ. As a result, the numerical system can be solved by the conventional finite element method, where model derivation is shown in Eqs. (24)–(28).

$$\int_{\Omega}\nabla W_{\varphi}\cdot\frac{1}{\rho}\nabla\varphi\ \mathrm{d}\Omega = \int_{\Gamma_{\mathrm{a}}} W_{\varphi}i_{\mathrm{a}}\mathrm{d}\Gamma + \int_{\Gamma_{\mathrm{c}}} W_{\varphi}i_{\mathrm{c}}\ \mathrm{d}\Gamma \tag{24}$$

$$\boldsymbol{K}_{\varphi}\boldsymbol{U}_{\varphi} = \boldsymbol{F}_{\varphi} \tag{25}$$

with

$$\boldsymbol{U}_{\varphi} = [\,\varphi_1 \quad \cdots \quad \varphi_{nn-1} \quad \varphi_{nn}\,] \tag{26}$$

$$\boldsymbol{K}_{\varphi} = \int_{\Omega}\boldsymbol{B}^{\mathrm{T}}\boldsymbol{D}_{\varphi}\boldsymbol{B}\ \mathrm{d}\Omega \tag{27}$$

$$\boldsymbol{F}_{\varphi} = \int_{\Gamma_{\mathrm{a}}}\boldsymbol{N}^{\mathrm{T}}i_{\mathrm{a}}\ \mathrm{d}\Gamma + \int_{\Gamma_{\mathrm{c}}}\boldsymbol{N}^{\mathrm{T}}i_{\mathrm{c}}\ \mathrm{d}\Gamma \tag{28}$$

where W_{φ} is the weighting function related to φ, $\boldsymbol{K}_{\varphi}$ and $\boldsymbol{F}_{\varphi}$ are stiffness matrix and force vector for φ analysis, respectively, $\boldsymbol{U}_{\varphi}$ is the vector that consists of nodal φ, and $\boldsymbol{D}_{\varphi} = \mathrm{diag}(1/\rho, 1/\rho)$ is the concrete conductivity matrix.

Nevertheless, the current-controlled analysis leads to an unconventional finite element system, consisting of the governing equation of V_{app} in Eq. (14), and the weak form of Eq. (24). To deal with this problem, the complex mathematical system is rearranged into two parts as:

$$Sub-system\ I:\quad \begin{cases} \displaystyle\int_{\Omega}\nabla W_{\varphi}\cdot\frac{1}{\rho}\nabla\varphi\ d\Omega \\ 0 \end{cases} = \begin{cases} \displaystyle\int_{\Gamma_{\mathrm{a}}} W_{\varphi}i_{\mathrm{a}}\ d\Gamma + \int_{\Gamma_{\mathrm{c}}} W_{\varphi}i_{\mathrm{c}}\ d\Gamma \\ 0 \end{cases} \tag{29a}$$

$$Sub-system\ II:\quad \begin{cases} 0 \\ \displaystyle\int_{\Gamma_{\mathrm{a}}} i_{\mathrm{a}}\ d\Gamma \end{cases} = \begin{cases} 0 \\ \displaystyle\int_{\Gamma_{\mathrm{a}}} i_{\mathrm{app}}\ d\Gamma \end{cases} \tag{29b}$$

In virtue of the division, the numerical system is allowed to be discretized sequentially. Galerkin method is first applied to the sub-system I, which, however, is hindered by the feature that V_{app} does not exhibit explicitly in the equation. In this regard, we further modify the sub-system I into Eq. (30).

$$\begin{aligned} &Sub-system\ I:\\ &\begin{cases} \displaystyle\int_{\Omega}\nabla W_{\varphi}\cdot\frac{1}{\rho}\nabla\varphi d\Omega \\ 0 \end{cases} = \begin{cases} \displaystyle\int_{\Gamma_{\mathrm{a}}} W_{\varphi}i_{\mathrm{a}}d\Gamma + \int_{\Gamma_{\mathrm{c}}} W_{\varphi}i_{\mathrm{c}}d\Gamma \\ 0 \end{cases}\\ &\Leftrightarrow \int_{\Omega}\nabla W_{\varphi}\cdot\frac{1}{\rho}\nabla\varphi + W_V\cdot 0\cdot V_{\mathrm{app}}d\Omega\\ &= \int_{\Gamma_{\mathrm{a}}} W_{\varphi}i_{\mathrm{a}} + W_V\cdot 0 d\Gamma + \int_{\Gamma_{\mathrm{c}}} W_{\varphi}i_{\mathrm{c}} + W_V\cdot 0 d\Gamma \end{aligned} \tag{30}$$

where W_V is the weighting function related to V_{app}.

In Eq. (30), the unknown variable V_{app} is defined as a global variable in this paper, which may cause numerical difficulty in discretizing sub-system I. To be more specific, the difference of the so-called global variable with other field variables is illustrated in Fig. 3. As shown in Fig. 3, the global variable is defined as a single valued constant throughout elements and not required to be interpolated based on nodal values by shape functions, which can be mathematically expressed as:

$$V_{\mathrm{app}} = U_{\mathrm{V}} \tag{31}$$

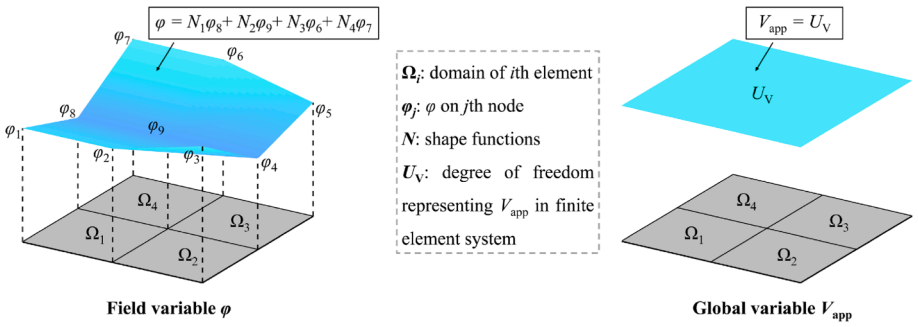

Fig. 3. Difference between the field and global variable.

where U_V is the degree of freedom representing V_{app} in the finite element system.

In order to handle the global variable in the same way as field variables, we freshly propose a pseudo discretization approach for V_{app}, in which Eq. (31) is logistically expanded to represent the φ-related degree of freedoms, see:

$$\begin{aligned} &V_{app} = U_V \\ &\Leftrightarrow V_{app} = 0\cdot\varphi_1 + \cdots + 0\cdot\varphi_{nn} + 1\cdot U_V = \boldsymbol{N}_V\cdot\widetilde{\boldsymbol{U}}_\varphi \end{aligned} \tag{32}$$

where $\boldsymbol{N}_V = [\boldsymbol{0}_{1\times nn}\ 1]$ is the shape function vector of the V_{app}, $\widetilde{\boldsymbol{U}}_\varphi = [\boldsymbol{U}_\varphi^T \quad U_V]^T$ is the vector consisting of all degree of freedoms in one finite element.

The discretized form for the sub-system I of Eq. (30) can be obtained by Galerkin method as:

$$\widehat{\boldsymbol{K}}_\varphi\widehat{\boldsymbol{U}}_\varphi = \widehat{\boldsymbol{F}}_\varphi \tag{33}$$

with

$$\widehat{\boldsymbol{K}} = \int_\Omega \widehat{\boldsymbol{B}}^T\widehat{\boldsymbol{D}}_\varphi\widehat{\boldsymbol{B}}\ \mathrm{d}\Omega \tag{34a}$$

$$\widehat{\boldsymbol{B}} = [\overline{\boldsymbol{B}}^T \quad \boldsymbol{N}_V^T]^T = \begin{bmatrix} \boldsymbol{B} & \boldsymbol{0}_{2\times1} \\ \boldsymbol{0}_{1\times nn} & 1 \end{bmatrix} \tag{34b}$$

$$\widehat{\boldsymbol{D}}_\varphi = \begin{bmatrix} \boldsymbol{D}_\varphi & \boldsymbol{0}_{2\times1} \\ \boldsymbol{0}_{1\times2} & 0 \end{bmatrix} \tag{34c}$$

$$\widehat{\boldsymbol{F}}_\varphi = \int_{\Gamma_a} \widehat{\boldsymbol{N}}^T\widehat{\boldsymbol{i}}_a^{\mathrm{I}}\ \mathrm{d}\Gamma + \int_{\Gamma_c} \widehat{\boldsymbol{N}}^T\widehat{\boldsymbol{i}}_c^{\mathrm{I}}\ \mathrm{d}\Gamma \tag{35a}$$

$$\widehat{\boldsymbol{N}} = [\overline{\boldsymbol{N}}^T \quad \boldsymbol{N}_V^T]^T = \begin{bmatrix} \boldsymbol{N} & 0 \\ \boldsymbol{0}_{1\times nn} & 1 \end{bmatrix} \tag{35b}$$

$$\widehat{\boldsymbol{i}}_a^{\mathrm{I}} = [i_a \quad 0]^T, \widehat{\boldsymbol{i}}_c^{\mathrm{I}} = [i_c \quad 0]^T \tag{35c}$$

where the sign ˆ means that the components correspond to the current-controlled analysis, with the consideration of the global variable. Except for the contribution to construct the equation system for finite element analysis, more importantly, the proposed pseudo discretization method can facilitate the solution of the highly nonlinear numerical system, which will be showcased in Section 3.3.

Following the discretization of sub-system I, the sub-system II should be modified correspondingly, as given in Eqs. (36)–(37).

$$\begin{cases} \boldsymbol{0}_{nn\times1} \\ \int_{\Gamma_a} i_a\ \mathrm{d}\Gamma \end{cases} = \begin{cases} \boldsymbol{0}_{nn\times1} \\ \int_{\Gamma_a} i_{app}\ \mathrm{d}\Gamma \end{cases} \Leftrightarrow \int_{\Gamma_a} \boldsymbol{i}_a^{\mathrm{II}}\ \mathrm{d}\Gamma = \int_{\Gamma_a} \boldsymbol{i}_{app}\ \mathrm{d}\Gamma \tag{36}$$

with

$$\boldsymbol{i}_a^{\mathrm{II}} = [\boldsymbol{0}_{1\times nn} \quad i_a]^T, \boldsymbol{i}_{app} = [\boldsymbol{0}_{1\times nn} \quad i_{app}]^T \tag{37}$$

As a result, we can write the complete system of equations for the current-controlled analysis to be solved by finite element method in Eq. (38).

$$\widehat{\boldsymbol{K}}_\varphi\widehat{\boldsymbol{U}}_\varphi + \int_{\Gamma_a} \boldsymbol{i}_a^{\mathrm{II}}\ \mathrm{d}\Gamma = \widehat{\boldsymbol{F}}_\varphi + \int_{\Gamma_a} \boldsymbol{i}_{app}\ \mathrm{d}\Gamma \tag{38}$$

3.3. Newton-Raphson method implementation

Newton-Raphson method [43,44], widely adopted for numerical simulations, is applied herein to solve the intended problem. Firstly, in terms of moisture transportation analysis, a modified method that eliminates nonlinearity and improves solution efficiency is used. To be specific, damping and stiffness matrices are estimated according to the previous time step, which has been proven effective in the authors' previous study [45], where the iteration procedure is given in Eq. (39).

$${}^{ii+1}\boldsymbol{U}_{RH} = {}^{ii}\boldsymbol{U}_{RH} - \boldsymbol{J}_{RH}^{-1}(\widetilde{\boldsymbol{K}}_{RH}\,{}^{ii}\boldsymbol{U}_{RH} - \widetilde{\boldsymbol{F}}_{RH}) \tag{39a}$$

$$\boldsymbol{J}_{RH} = \widetilde{\boldsymbol{K}}_{RH} = \boldsymbol{M}_{RH}(\overleftarrow{\boldsymbol{U}}_{RH}) + \Delta t\boldsymbol{K}_{RH}(\overleftarrow{\boldsymbol{U}}_{RH}) \tag{39b}$$

where ii indicates the iith iteration, $\boldsymbol{J}_{RH}$ is the Jacobian for solving the *RH* field.

On the other hand, nonlinearity exists in the boundary condition for corrosion analysis, preventing the application of modified Newton-Raphson method. Therefore, the classical iteration process is implemented, where the solution processes for the voltage-controlled and current-controlled analysis are listed in Eq. (40) and Eq. (41), respectively.

$${}^{jj+1}\boldsymbol{U}_\varphi = {}^{jj}\boldsymbol{U}_\varphi - \boldsymbol{J}_\varphi^{-1}(\boldsymbol{K}_\varphi\,{}^{jj}\boldsymbol{U}_\varphi - \boldsymbol{F}_\varphi) \tag{40a}$$

$$\boldsymbol{J}_\varphi = \boldsymbol{K}_\varphi - \frac{\partial\boldsymbol{F}_\varphi}{\partial\boldsymbol{U}_\varphi} \tag{40b}$$

$${}^{jj+1}\widehat{\boldsymbol{U}}_\varphi = {}^{jj}\widehat{\boldsymbol{U}}_\varphi - \widehat{\boldsymbol{J}}_\varphi^{-1}(\widehat{\boldsymbol{K}}_\varphi\,{}^{jj}\widehat{\boldsymbol{U}}_\varphi + \int_{\Gamma_a} \boldsymbol{i}_a^{\mathrm{II}}\ \mathrm{d}\Gamma - \widehat{\boldsymbol{F}}_\varphi - \int_{\Gamma_a} \boldsymbol{i}_{app}\ \mathrm{d}\Gamma) \tag{41a}$$

$$\widehat{\boldsymbol{J}}_\varphi = \widehat{\boldsymbol{K}}_\varphi + \int_{\Gamma_a} \frac{\partial\boldsymbol{i}_a^{\mathrm{II}}}{\partial\widehat{\boldsymbol{U}}_\varphi}\ \mathrm{d}\Gamma - \frac{\partial\widehat{\boldsymbol{F}}_\varphi}{\partial\widehat{\boldsymbol{U}}_\varphi} \tag{41b}$$

where jj indicates the jjth iteration, $\boldsymbol{J}_\varphi$ and $\widehat{\boldsymbol{J}}_\varphi$ are Jacobians for the voltage-controlled and current-controlled analysis, respectively.

By evaluating Eqs. (40)–(41), the accurate representation of partial deviation terms is essential to the solution. Attributing to the pseudo discretization approach as introduced for the global variable, these terms for both current-controlled and voltage-controlled analyses can be derived in a straightforward manner in Eqs. (42)–(43).

$$\frac{\partial\boldsymbol{F}_\varphi}{\partial\boldsymbol{U}_\varphi} = \int_{\Gamma_a} \boldsymbol{N}^T\frac{\partial i_a}{\partial\varphi}\boldsymbol{N}\ \mathrm{d}\Gamma + \int_{\Gamma_c} \boldsymbol{N}^T\frac{\partial i_c}{\partial\varphi}\boldsymbol{N}\ \mathrm{d}\Gamma \tag{42}$$

$$\int_{\Gamma_a} \frac{\partial \dot{i}_a^{II}}{\partial \widehat{U}_\varphi} \, d\Gamma = \int_{\Gamma_a} \frac{\partial \dot{i}_a^{II}}{\partial Y} \widehat{N} \, d\Gamma \, , \; Y = [\varphi \quad V_{app}]^T \tag{43a}$$

$$\frac{\partial \widehat{F}_\varphi}{\partial \widehat{U}_\varphi} = \int_{\Gamma_a} \widehat{N}^T \frac{\partial \widehat{i}_a^{I}}{\partial Y} \widehat{N} \, d\Gamma + \int_{\Gamma_c} \widehat{N}^T \frac{\partial \widehat{i}_c^{I}}{\partial Y} \widehat{N} \, d\Gamma \tag{43b}$$

4. Model validations

4.1. Problem descriptions

Two accelerated experiments with constant i_{app} of 250 $\mu A/cm^2$ as reported by Fu et al. [29] and Chen et al. [30] are investigated herein to validate the effectiveness of the proposed algorithm, where the schematic experimental setups are illustrated in Fig. 4.

In Fu et al. [29], a cylindrical specimen is exposure to the air for 2 days, where an embedded stainless-steel wire functions as the cathode. Different from this air-exposed method, Chen et al. [30] connected a fully immersed reinforced concrete block to an auxiliary electrode through the power source for 22 days. According to the literature [46,47], steel depassivation occurs with chloride ingress, which can be presented by a gradual reduction of β_{Fe}. In both experimental studies, the samples were submerged in NaCl solution for a long period before impressing current to ensure concrete saturation and complete steel depassivation. By doing so, the modelling of depassivation process of reinforcement can be ignored, where chloride penetration is not required to be considered in numerical studies.

Despite the identical anodic iron dissolution reaction as shown in Eq. (44), different experimental settings could result in different cathodic reactions. In the experiment of Fu et al. [29], considerable oxygen reduction reaction happens on cathode due to the sufficient oxygen supply from the atmosphere. On the contrary, the oxygen availability in the study designed by Chen et al. [30] is hindered by the surrounding solution, where the hydrogen evolution reaction dominates instead. Cathodic reactions in these two electrochemical systems are summarized in Eq. (45), and electrochemical parameters for fully depassivated reinforcement are listed in Table. 1 [45,48]. Note that subscripts Fe, O_2 and H_2 denote iron dissolution reaction, oxygen reduction reaction and hydrogen evolution reaction respectively (Fu et al. [29]) (Chen et al. [30]).

$$Fe - 2e^- = Fe^{2+} \tag{44}$$

$$O_2 + 4e^- + 2H_2O = 4OH^- \tag{45a}$$

$$2H_2O + 2e^- = H_2 + 2OH^- \tag{45b}$$

Table 1
Electrochemical parameters of electrode reactions for validation.

Exchange current density (A/m^2)			*Equilibrium potential* (V vs. SCE)			*Tafel's slope* (V/dec)		
i^0_{Fe} [45]	$i^0_{O_2}$ [45]	$i^0_{H_2}$ [48]	E_{Fe} [45]	E_{O_2} [45]	E_{H_2} [48]	β_{Fe} [45]	β_{O_2} [45]	β_{H_2} [48]
3×10^{-4}	1×10^{-5}	1.1×10^{-2}	−0.68	0.16	−0.95	0.09	−0.18	−0.15

Based on the proposed algorithm, two-dimensional finite element analyses are implemented, where bilinear quadrilateral (Q4) elements are employed for meshing. In terms of the experiment of Fu et al. [29], the minimum and maximum element size are defined as $4e^{-4}$ mm and 0.2 mm respectively, where 8671 elements are generated. Moreover, 11,450 elements are applied to model the experiment of Chen et al. [30] by setting the minimum and maximum element size as $3.2e^{-3}$ mm and 1.5 mm respectively.

4.2. Accelerated corrosion under air-exposed condition

To achieve precise modelling results, convergence performance of the solution algorithm is evaluated first. Given that the model cannot be solved analytically, the numerical solution with 5-min time step is taken as the reference for assessment. Compared to the reference, the convergence of the algorithm against various time stepping choices is assessed by the coefficient of determination (R^2) in Eq. (46).

$$R^2 = 1 - \frac{\left\| \boldsymbol{U} - \boldsymbol{U}_{ref} \right\|^2}{\left\| \boldsymbol{U}_{ref} - \overline{U}_{ref} \right\|^2} \tag{46}$$

where $\|\cdots\|$ is the 2-norm of a vector, $\boldsymbol{U}$ and $\boldsymbol{U}_{ref}$ are the investigated solution vector and reference solution vector, respectively, $\overline{U}_{ref}$ is the mean of the reference solution vector.

The convergence performance of the algorithm is shown in Fig. 5, where the solution converges gradually with decreasing time step. To be more specific, the marginal modelling precision loss is achieved by the 2-hour time step, which is indicated by a value of R2 close to 1. Therefore, the 2-hour time step is adopted in the following analyses.

After the convergence study, the corrosion propagation in the experiment of Fu et al. [29] is simulated by the algorithm, with the environmental RH of 50% as the boundary condition. However, rather than the corrosion rate, the reported corrosion response in the experiment is the final rust thickness on the rebar surface, which was measured on several cross sections to consider the material heterogeneity. In the

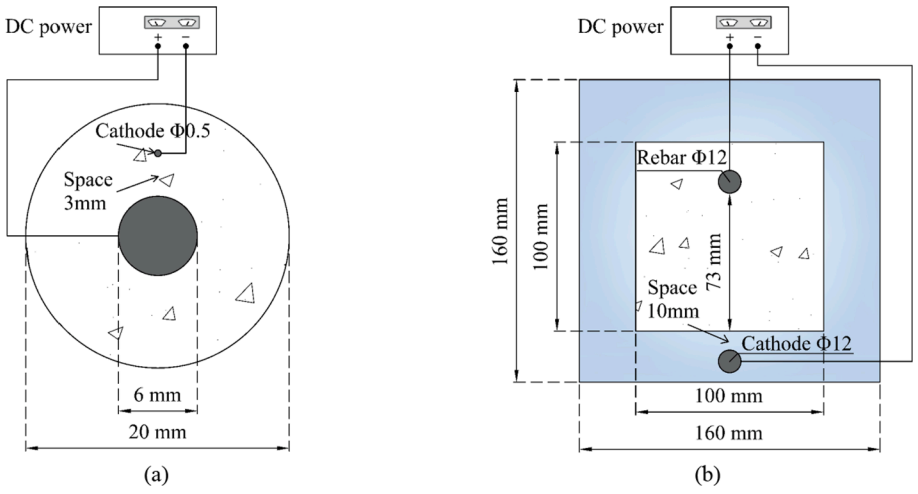

Fig. 4. Schematic experimental setups from: (a) Fu et al. [29]; (b) Chen et al. [30].

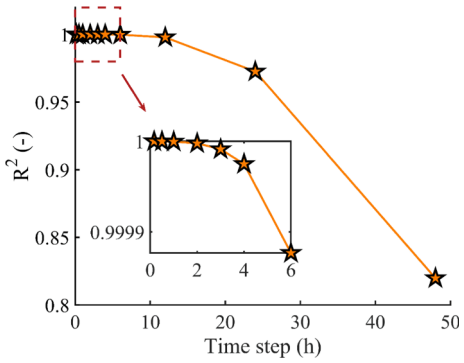

Fig. 5. Convergence plot of the algorithm.

numerical study, Faraday's law of Eq. (47) is employed for the calculation of rust thickness [49], where the simulated and experimental results are compared in Fig. 6.

$$r(t) = \frac{nA_{\mathrm{Fe}} \int_0^t i_{\mathrm{Fe}} \mathrm{d}t}{z_{\mathrm{Fe}} \mathrm{F} \rho_{\mathrm{S}}} \tag{47}$$

where $r(t)$ is the rust thickness (m) on rebar surface at the time t (s), n is the rust expansion coefficient (-), A_{Fe} is the molar mass of iron (g/mol), z_{Fe} is valency (-) of iron dissolution reaction, ρ_{S} is the mass density of steel (g/m^3). In the present modelling, n is assumed to be 3.55.

According to Fig. 6, the simulated result well respects the measured rust thickness, which manifests the competence of the proposed solution method. Either in the modelling or the experiment, the highly localized corrosion pattern generated by this corrosion acceleration method is revealed. The corrosion degree of rebar depends on the distance away from the stainless-steel wire, where more severe corrosion is observed for the spot closer to the cathode. Generally, the cathode-facing side of the steel interacts with the cathode more actively, leading to significant rust accumulation. Furthermore, inhomogeneous concrete resistivity induced by the gradual drying of the specimen intensifies the corrosion nonuniformity. To validate this claim, the streamline of current density at the end of testing duration is numerically obtained in Fig. 7 to visualize current paths between electrodes. Moreover, by choosing several moments, the time-variant concrete resistivity is evaluated and shown in Fig. 8.

As shown in Fig. 8, the concrete resistivity is unevenly distributed, and the nonuniformity is gradually alleviated with the reducing moisture difference between the material and the exterior atmosphere. Noticeably, throughout the air-exposed experiment, the resistivity of the concrete core is constantly smaller than that of the outer layer. By examining Fig. 7, the streamline of current density between the upper part of the steel and cathode mainly locates at the low resistivity region, which facilitates the corrosion by the reduced energy consumption in

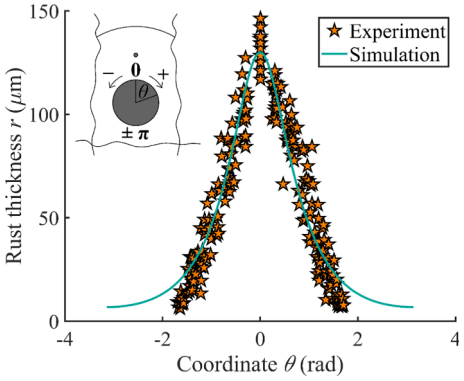

Fig. 6. Comparison of simulated and experimental rust thickness r at day 2.

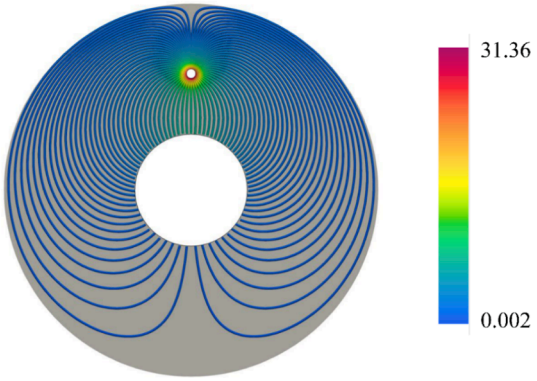

Fig. 7. Streamline of current density in concrete at the end of experiment (A/m^2).

the galvanic coupling. It is demonstrated that the localized corrosion pattern is controlled by the combined effect of length and resistivity of current paths between electrodes.

4.3. Accelerated corrosion under immersed condition

The numerical approach is further validated against the experiment of Chen et al. [30], where the resistivity of solution is assumed as 1 Ω·m. Despite that Faraday's law is stilled followed to estimate the rust thickness, the fitted rust expansion coefficient of 3.15 in the present experiment is slightly smaller than the fitted value in the previous experiment. This distinction can be explained by the different exposure conditions, as the parameter is indeed susceptible to the environment in concrete [50,51]. The comparison of the modelled and experimental-measured rust thickness is shown in Fig. 9, where the modelled corrosion rate is also illustrated. The concrete and solution resistivity remain constant throughout the immersed experiment, hence the corrosion rate in Fig. 9 corresponds to any point in time throughout the experiment.

According to Fig. 9, the modelling result agrees well with the measured rust accumulation at the end of the test. Different from the experiment of Fu et al. [29], both the rust and corrosion rate along the rebar surface only present slight nonuniformity in the soaking setting. The other noticeable difference is that the lower part of the rebar is less corroded than the upper part, in spite of being closer to the auxiliary electrode. To further investigate such an uncharacteristic finding, the streamline of current density during the accelerated corrosion experiment is numerically obtained in Fig. 10.

Fig. 10 illustrates that the current flows from the anode to the cathode through both concrete and the surrounding solution. While the lower part of the rebar interacts with the auxiliary electrode by the current in the concrete, the upper part mainly relies on the current in the solution. As shown in Fig. 10, the magnitude of current flowing in the solution is remarkably greater than that in the concrete, which coincides with the fact that solution resistivity is much lower than concrete resistivity. Despite the fact that the current path between the upper rebar and the cathode is longer, power consumption in the path tends to be less due to smaller overall resistivity. In this regard, a more serious corrosion status is observed at the upper part of the rebar in Fig. 9. Moreover, due to the constant resistivity of the corrosion cell, a specific relation exists between the intended corrosion rate and required power supply in the fully immersed experiment. By taking advantage of the proposed algorithm, the correlation is determined for the investigated experiment in the present study, see Fig. 11.

The relation between the applied voltage and rebar corrosion rate is illustrated in Fig. 11, which can be established by either a series of voltage-controlled or current-controlled studies. This finding not only verifies the authors' claim, but also demonstrates the consistency between the voltage-controlled and current-controlled corrosion analysis

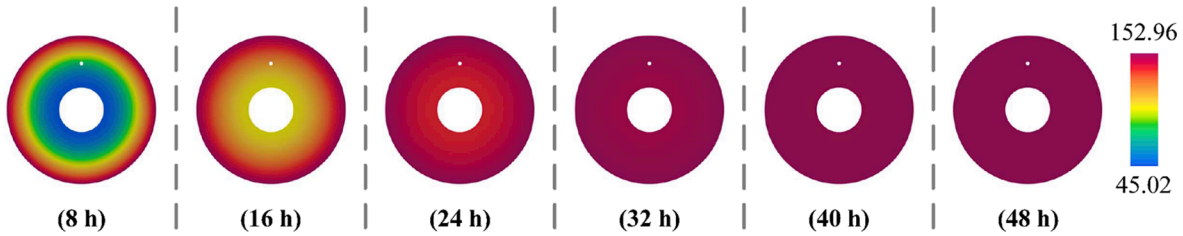

Fig. 8. Time-dependent change of concrete resistivity distribution (Ω·m).

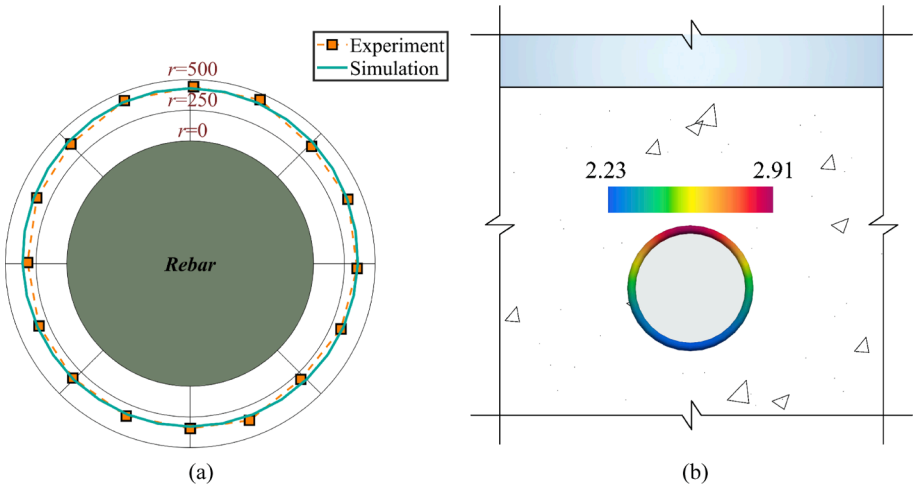

Fig. 9. (a) Comparison of simulated and experimental rust thickness r at day 22 (μm); (b) simulated corrosion current density distribution along rebar surface i_{Fe} (A/m^2).

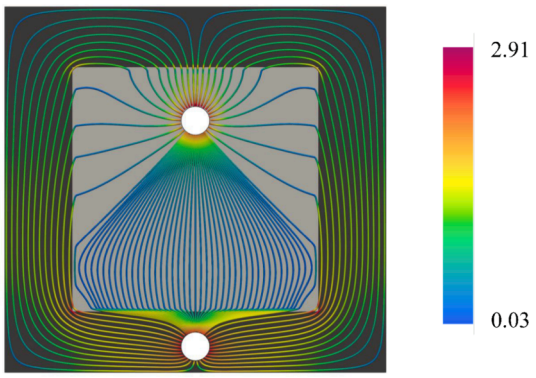

Fig. 10. Streamline of current density in concrete and surrounding solution (A/m^2).

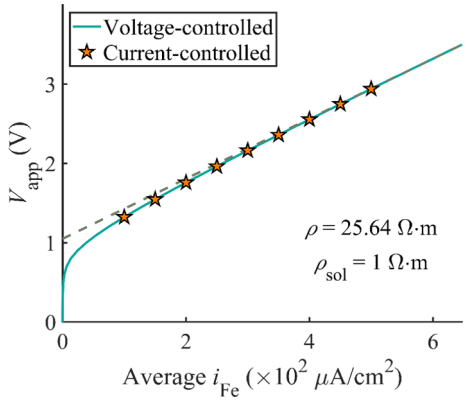

Fig. 11. Relation between the power supply and rebar corrosion.

by using the proposed algorithms. Interestingly, the rebar corrosion does not initiate in a weak power source, as the hydrogen evolution reaction on the cathode can only be stimulated by a strong electric field [48]. The other significant discovery is that the applied voltage and the acceleration effect correlates linearly in the range of high voltage, which is of potential to provide guidance for the design of a similar type of accelerated experimentation.

5. Analyses and discussions

5.1. Problem descriptions

Several numerical cases are designed for comprehensively investigating the influence of steel depassivation status on the effectiveness of cathodic protection for aging structures. A circular reinforced concrete specimen with initial *RH* of 80%, resembling the pier of aging bridges, is applied in the analyses [52], where 12 rebars evenly distribute along the circumference. The specimen is subjected to the atmosphere with *RH* of 30% for a period of 120 days to generate continuous variation in saturation degree, see Fig. 12. A layer of zinc, which can be used for both sacrificial anode cathodic protection (SACP) and ICCP [53], is placed over the concrete exterior surface to protect reinforcements. In engineering practice, a typical example of such a measure is the Depoe Bay Bridge located in the United States, where 5900 m^2 of zinc anode was adopted through thermal spray [54], see Fig. 13.

Generally, reinforcement depassivation occurs from the spot closest to the exposure surface due to the gradual chloride ingress [55], where continuous localized corrosion occurs. As the focal point of present study is the steel status when the cathodic protection employs, detailed modelling of chloride ingress and the depassivation process is ignored. In this regard, the depassivation status is indicated by the area of steel depassivation zone using an angle α, see Fig. 12. In the present study, the

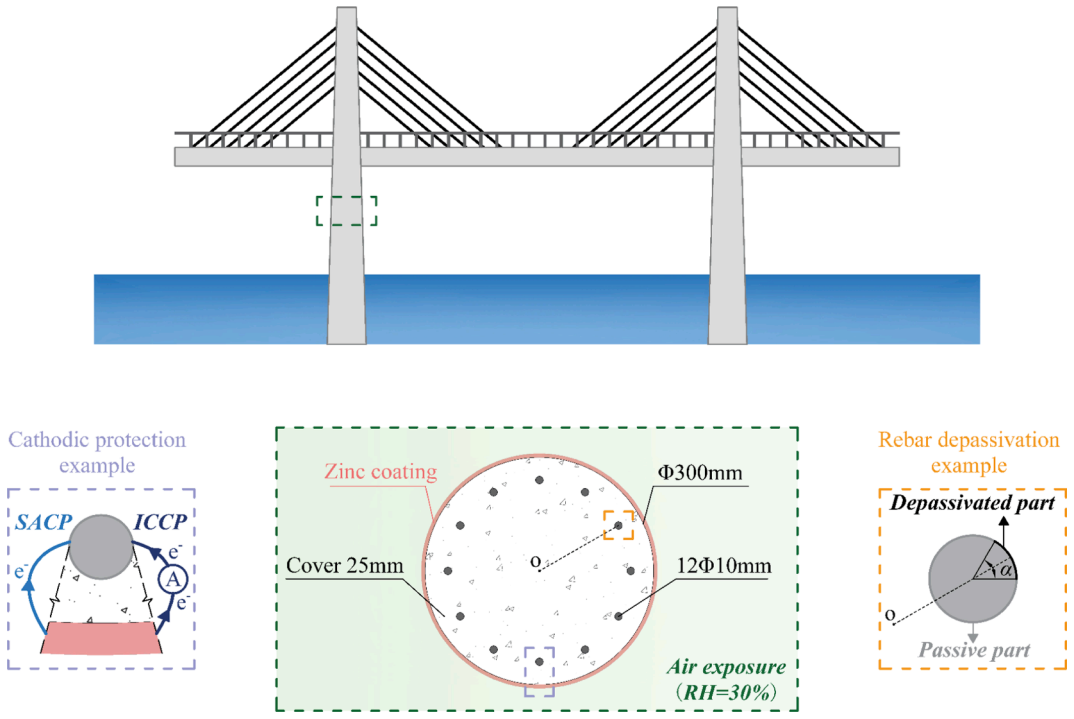

Fig. 12. Reinforced concrete specimen for the numerical analysis.

Fig. 13. Depoe Bay Bridge with thermally spayed zinc over the surface (picture from [56]).

investigated angle ranges from 40° to 160° with an interval of 20°.

In the cathodic protection system, zinc is sacrificed to mitigate the rebar corrosion. Three different electrode reactions are considered on the steel surface, encompassing iron dissolution reaction, oxygen reduction reaction and hydrogen evolution reaction. Most of the electrochemical parameters for these reactions follow the Table. 1, expect for β_{Fe}. Depending on the steel depassivation state, β_{Fe} are defined as 0.09 and 3 for the active part and the passive part in the present study, respectively. Moreover, the zinc-supplied protection current density is essential to the modelling, which is estimated by a Butler-Volmer type equation presented in Eq. (48) [40], and treated as two superimposed Tafel's equations. Electrochemical parameters for the anode are summarized in Table. 2. Following the necessary parameters, two-dimensional finite element analyses are conducted, where the mesh is composed of 6493 elements, with densification near the exposure surface.

Table 2
Electrochemical parameters for zinc anode [40].

$i_a^0\left(A/m^2\right)$	E_a(V vs. SCE)	β_a^{ox}(V/dec)	β_a^{red}(V/dec)
4e-3	−1.01	0.019	−0.05

$$i_a = i_a^0\{\exp[\frac{2.303(V_{app}-\varphi-E_a)}{\beta_a^{ox}}] - \exp[\frac{2.303(V_{app}-\varphi-E_a)}{\beta_a^{red}}]\} \quad (48)$$

where i_a^0 is the exchange current density (A/m^2), E_a is the equilibrium potential (V vs. SCE), β_a^{ox} and β_a^{red} are the Tafel's slope for the oxidation and reduction reaction on the zinc anode, respectively.

5.2. Rebar corrosion without cathodic protection

To investigate the necessity of cathodic protection measures for the aging structure, natural corrosion is evaluated first. In engineering practice, the most common experimental technique in corrosion assessment is the polarization resistance method [45], where the average corrosion current density over the rebar is measured. In this regard, taking advantage of the proposed method, the average corrosion rate without protection is numerically obtained in Fig. 14.

As shown in Fig. 14, the average corrosion rate increases as the depassivation progresses, which is consistent with the well-recognized corrosion propagation process [57]. It is also noticed that the corrosion gradually decelerates as the atmospheric exposure. To explain the phenomenon, changes of RH and corresponding concrete resistivity are evaluated in Fig. 15. As shown in Fig. 15, as the progressive increase of the resistivity with continuous drying, there witnesses a reduction in terms of interaction between active and passive steel, hence the decrease of corrosion rate. Moreover, it is recognized that the average response cannot fully depict the detailed corrosion intensity [45], and the maximum corrosion rate of the reinforcements is further investigated in Fig. 16.

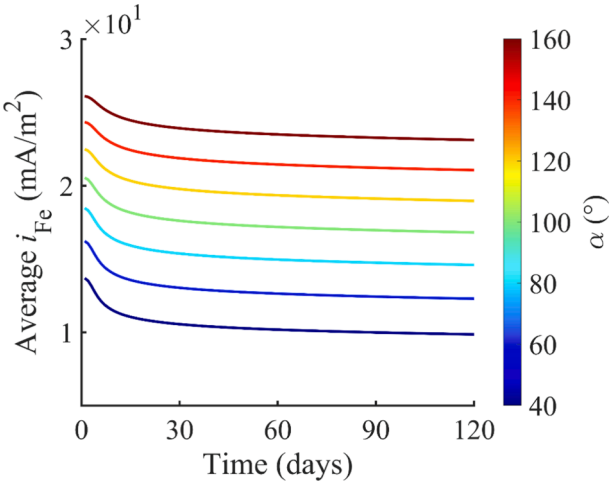

Fig. 14. Average corrosion rate of the aging structure without cathodic protection.

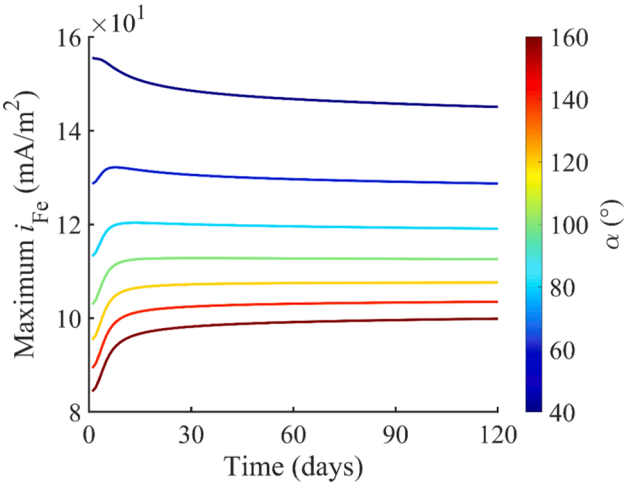

Fig. 16. Maximum corrosion rate of the aging structure without cathodic protection.

Fig. 16 shows that the maximum corrosion rate of the reinforcements far exceeds the average rate, which verifies the above claim. Despite that the average corrosion rate increases with the gradual steel depassivation, higher maximum corrosion rate is observed in more severely localized corrosion. Moreover, as concrete drying proceeds, the monotonic decreasing trend of corrosion rate as indicated by average corrosion rate is absent when examining the maximum current density. To be more specific, the decreasing tendency is only witnessed in the activation zone with α of 40°, while the corrosion rate and the saturation degree gradually becomes inversely correlated with the progressive depassivation. This interesting finding can be explained by evaluating the effects of concrete saturation degree. The drying can lead to not only deceleration of the overall corrosion process, but also shift of corrosion towards the intersection between active and passive steel. In fact, as shown in Fig. 17, the intersection part is where maximum current density appears. These two opposite effects on maximum corrosion rate vary with steel depassivation states, resulting in a complicated relation between the corrosion rate and concrete saturation degree.

According to the literature [35,45], active corrosion propagation is widely considered to proceed when measured corrosion current density is greater than the critical value of 1 mA/m^2. Herein, despite that different characteristics are observed in Fig. 14 and Fig. 16, the average and maximum corrosion rates are both much larger than the critical corrosion rate during the exposure period. Therefore, the cathodic protection method is necessary to be implemented to ensure the safety of aging structures. Moreover, aiming at the overall protection of rebars, the maximum corrosion rate is employed to evaluate the protection performance in the following discussions, where the complete protection is indicated by a corrosion rate smaller than 1 mA/m^2.

5.3. Rebar corrosion with SACP and voltage-controlled ICCP

To mitigate the severe corrosion issue in aging structures, the zinc layer is installed to interfere with the electrochemical system. The protection effect without impressed current is investigated first, where the external power supply is in an open circuit state to produce SACP, i.e., V_{app} = 0V. By taking two specific depassivation state as example, i.e., activation zones with α of 40° and 160°, the current flow in the SACP is shown in Fig. 18.

Fig. 18 illustrates the protection current flowing from the zinc layer to the reinforcements in the concrete, which complies with the principle of SACP [58]. To assess the performance of SACP, the maximum steel

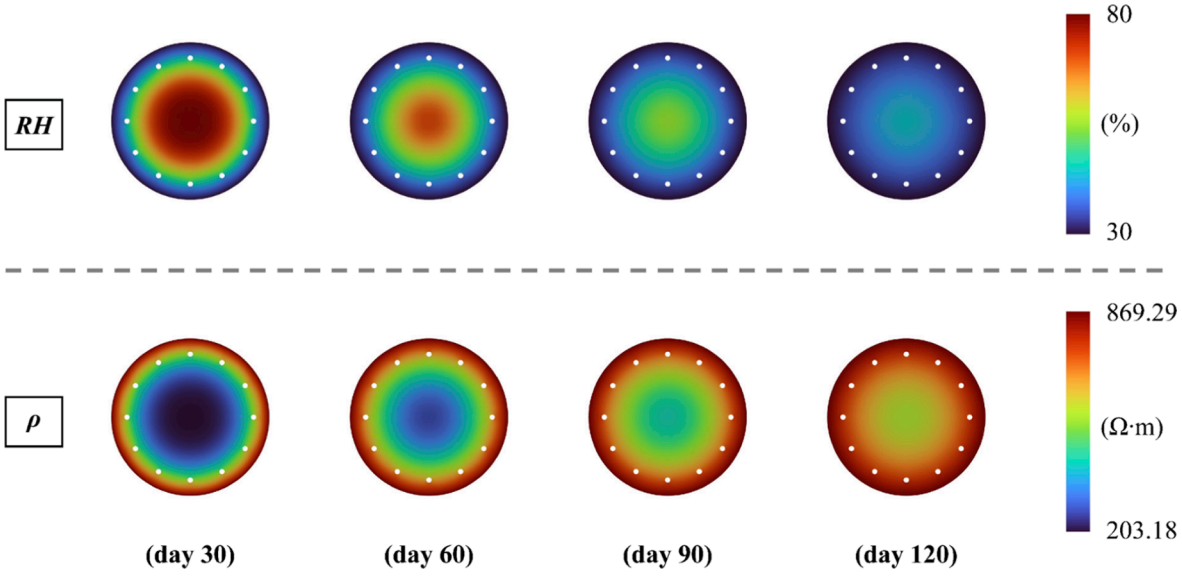

Fig. 15. Time-dependent change of *RH* and concrete resistivity.

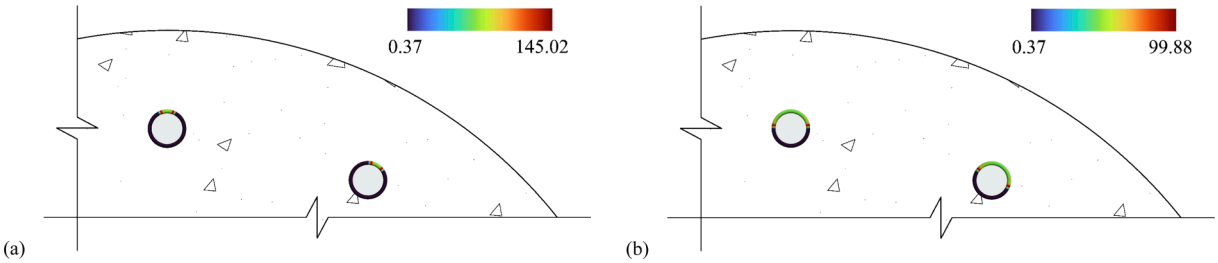

Fig. 17. Corrosion current density (mA/m^2) distribution along rebar surface at the end of exposure: (a) $\alpha = 40°$; (b) $\alpha = 160°$.

corrosion rate throughout the exposure period is showcased in Fig. 19. Despite that higher corrosion localization leads to larger maximum corrosion rate in the natural scenario, the stronger localized corrosion can be arrested by SACP more effectively, as illustrated in Fig. 19. However, the fact that maximum corrosion rate of all reinforcements is always greater than 1 mA/m^2 manifests the deficiency of SACP, thus power supply should be connected to perform ICCP.

The voltage-controlled technique is first applied to the power supply of ICCP. For thorough efficacy investigation, a series of numerical studies with constant V_{app} ranging from 0.5 V to 3 V with an interval of 0.5 V are conducted, where the corrosion responses of reinforcements are shown in Fig. 20.

According to Fig. 20, generally, the corrosion of steel with smaller depassivation extent can be restrained by voltage-controlled ICCP more effectively. Throughout the exposure period, while the steel with activation zone α of 40° is completely protected by ICCP using controlled voltage of 2 V, the required voltage raises to 3 V for the steel with activation zone α of 160° for maintaining an effective protection. For ICCP controlled in voltage greater than 1.5 V, however, a stage when the protection effectiveness is independent of the steel depassivation state is observed in the early exposure, where the duration of the stage increases with the enhancing power source. The influence of concrete saturation state on voltage-controlled ICCP is also illustrated in Fig. 20. It is evident that the protection performance reduces with the gradual concrete drying. This phenomenon is caused by the decreasing protection current

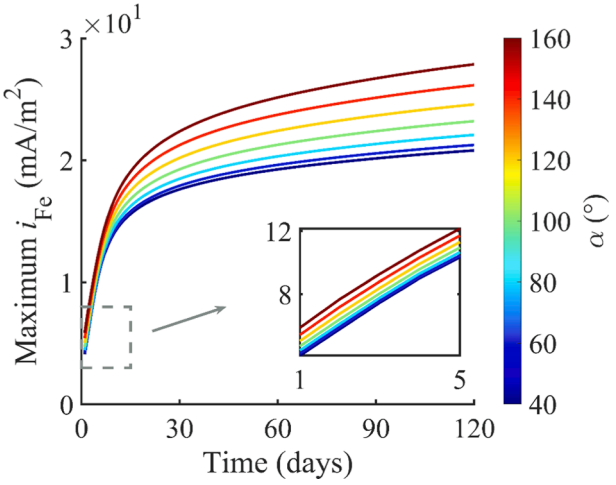

Fig. 19. Maximum steel corrosion rate with different α in SACP.

provided by zinc anode under the progressively increasing concrete resistivity, see Fig. 21. It is worth mentioning that only the case with α of activation zone = 40° is illustrated in Fig. 21 to ease the writing, where the effect of depassivation state on the current is marginal based on the numerical investigation.

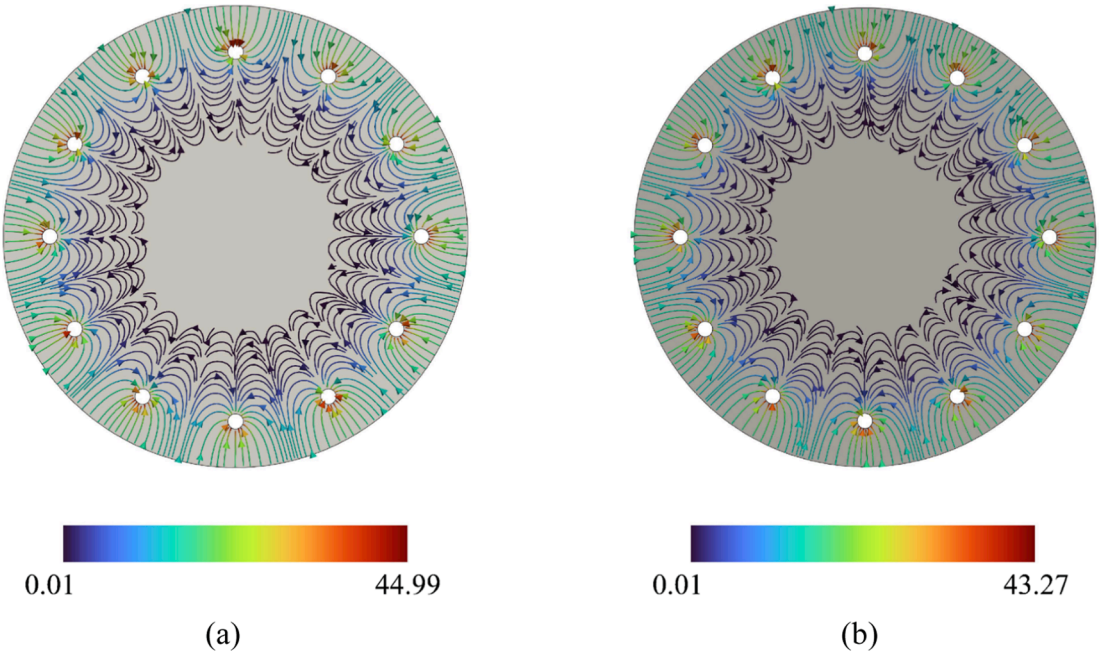

Fig. 18. Streamline of current density (mA/m^2) in concrete at Day 120: (a) $\alpha = 40°$; (b) $\alpha = 160°$.

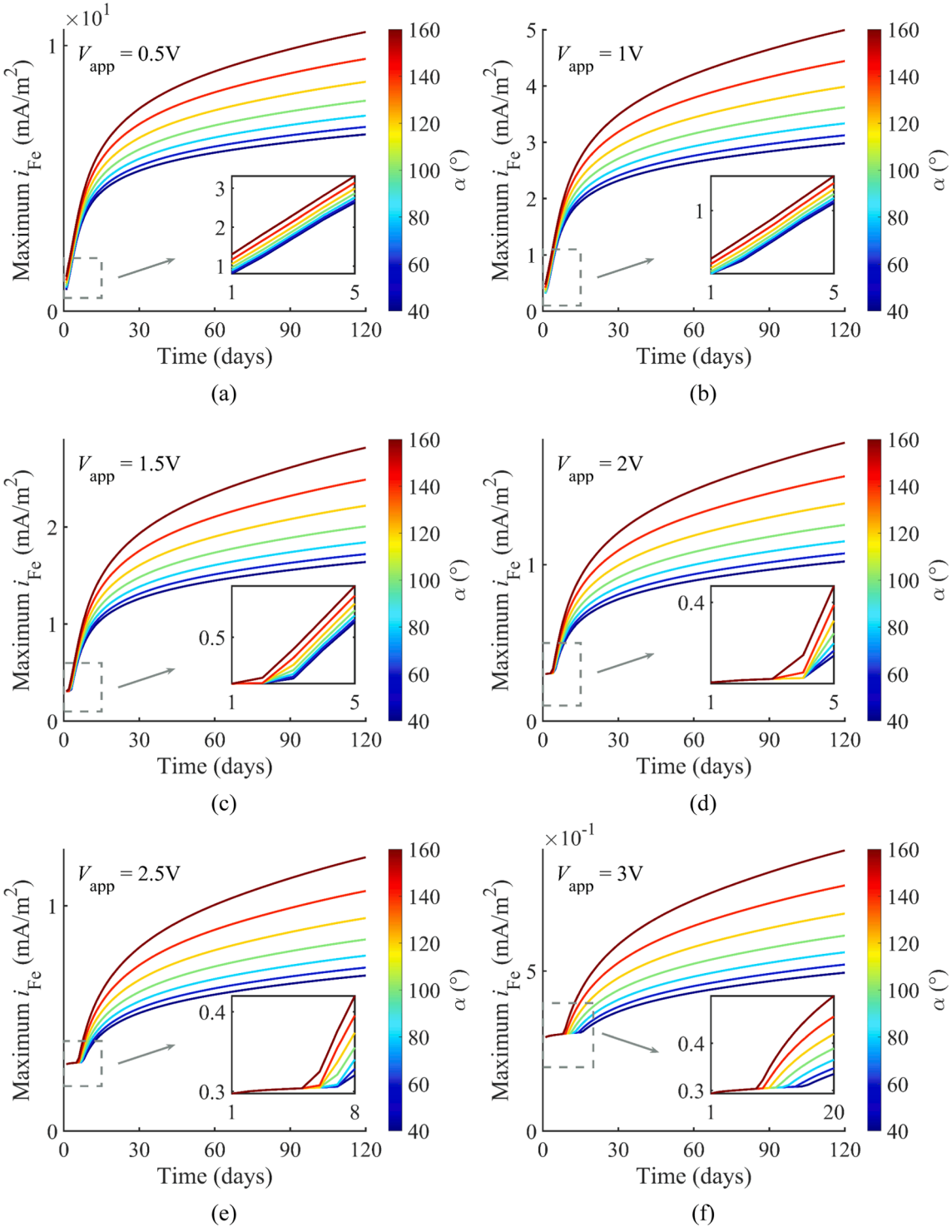

Fig. 20. Maximum steel corrosion rate with different α in voltage-controlled ICCP: (a) 0.5 V; (b) 1 V; (c) 1.5 V; (d) 2 V; (e) 2.5 V; (f) 3 V.

5.4. Rebar corrosion with current-controlled ICCP

In this section, the proposed algorithm is further applied to examine the effectiveness of current-controlled ICCP. To be specific, the protection current density provided by zinc anode, i.e., i_{app}, is kept as constants in numerical studies, ranging from 40 mA/m^2 to 100 mA/m^2 with an interval of 20 mA/m^2. The protection performances of current-controlled ICCP are shown in Fig. 22.

According to Fig. 22, the anti-corrosion performance of current-controlled ICCP is more remarkable for steel with smaller depassivation area, which is consistent with the general trend found in SACP and voltage-controlled ICCP. Therefore, the effectiveness of a cathodic protection system is dependent not only on the volume of the protected structures [59], but also on the depassivated state of the protected structure, which should be considered in engineering practice. Moreover, concrete drying leads to a complicated variation in protection effectiveness of current-controlled ICCP. To explain this interesting phenomenon, current-controlled ICCP is sketched in Fig. 23.

As illustrated in Fig. 23, in current-controlled ICCP, constant number of electrons transport from the zinc coating to the steel through the

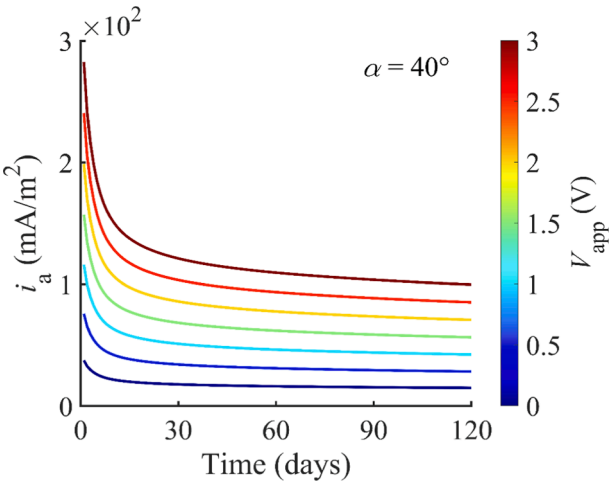

Fig. 21. Change of protection current density provided by zinc anode in voltage-controlled ICCP.

external circuit, i.e., wires, under the effect of power supply. Meanwhile, due to the macrocell corrosion, electrons are released by the depassivated steel and accumulate on the passive steel, which stimulates the zinc-provided electrons towards the corroding part. In the early exposure phase, the influence recedes due to the concrete drying-induced macrocell corrosion mitigation [60], leading to the protection level reduction. Nevertheless, as drying proceeds, the protection current received by the zinc anode-facing depassivated steel augments [61] for lessening the power consumption in the internal circuit, i.e., concrete. In consequence, following the initial decreasing stage, protection performance exhibits an increasing trend, see Fig. 22. With the enlarging activated area of steel, it is observed that the competed effects of concrete drying gradually balance in the later exposure phase. It may be caused by less electron accumulation on passive steel due to the domination of microcell corrosion, as well as the longer distance between the most corroded spot and zinc anode.

6. Conclusions

In this work, a robust finite element-based algorithm is developed for analyzing corrosion propagation of reinforced concrete structures under external power supply, where a novel pseudo discretization approach is introduced for the global variable in the current-controlled analysis. The Newton-Raphson method is exploited to solve the highly nonlinear numerical system. In virtue of the staggered solution scheme, the effect of the moisture transportation on the corrosion process is considered as well. The proposed method is validated against reported accelerated corrosion experiments. Furthermore, the performance of SACP and ICCP on the reinforced concrete specimen is assessed, in which the influence of steel depassivation extent and concrete saturation state is clarified. The following significant insights are summarized through the numerical investigations:

1. The steel corrosion pattern generated in the accelerated corrosion experiments is significantly impacted by the experimental setups, where the air-exposure method generates more localized corrosion than the soaking method.

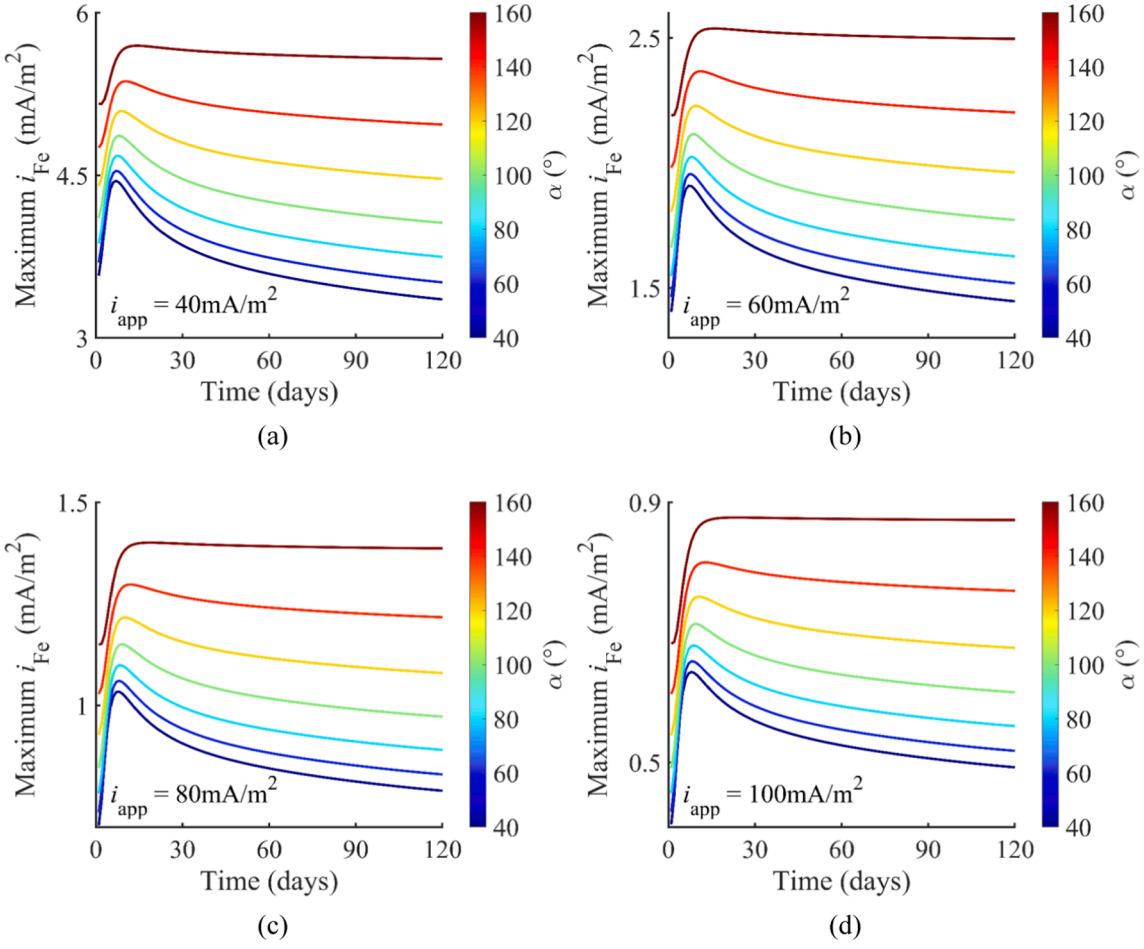

Fig. 22. Maximum steel corrosion rate with different α in current-controlled ICCP: (a) 40 mA/m^2; (b) 60 mA/m^2; (c) 80 mA/m^2; (d) 100 mA/m^2.

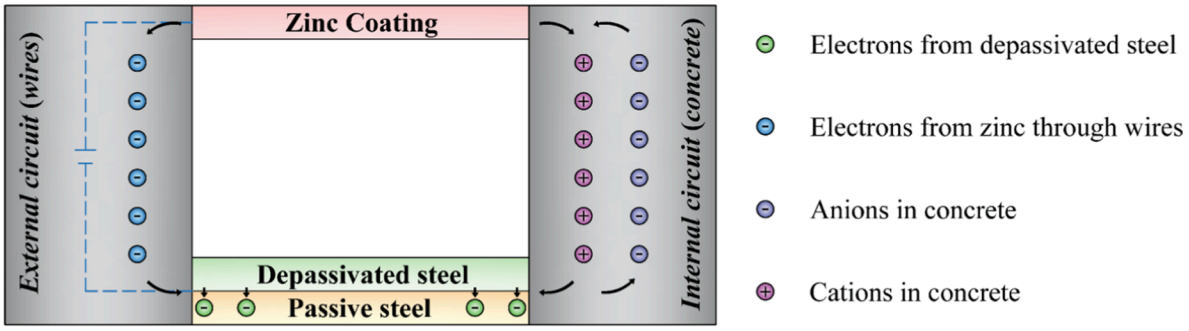

Fig. 23. Schematic drawing of current-controlled ICCP.

2. ICCP can mitigate the corrosion of reinforcements more effectively than the SACP, and the performance of ICCP improves with the enhancement of power supply.
3. The performances of both current-controlled and voltage-controlled ICCP are dependent on the steel depassivation state. To be specific, the corrosion of steel with smaller activation area is easier to prevent, even though higher maximum corrosion rate is observed before the anti-corrosion measure.
4. The effects of concrete saturation state on voltage-controlled and current-controlled ICCP are different. While the protection level provided by voltage-controlled ICCP decreases as concrete drying, an increasing trend of current-controlled ICCP performance is found after the initial decline stage.

Overall, the proposed solution strategy can be expanded to more complex corrosion models in a straightforward manner, where reinforcement depassivation with chloride ingress and variations in electrochemical properties can be considered under the effect of power supply. By doing so, further studies are expected to enrich the understanding regarding the efficiency of accelerated corrosion experiments and the effect of cathodic protection on reinforcement depassivation state. Therefore, the current work plays a backbone role in solving power supply-involved corrosion problems.

CRediT authorship contribution statement

Bin Dong: Conceptualization, Formal analysis, Methodology, Validation, Writing – original draft. **Yuguo Yu:** Supervision, Writing – review & editing. **Yuan Feng:** Supervision. **Di Wu:** Supervision. **Gaofeng Zhao:** Supervision. **Airong Liu:** Supervision. **Wei Gao:** Funding acquisition, Supervision, Writing – review & editing.

Declaration of Competing Interest

The authors declare that they have no known competing financial interests or personal relationships that could have appeared to influence the work reported in this paper.

Data availability

Data will be made available on request.

Acknowledgements

The research work presented in this paper has been supported by Australian Research Council project IH200100010, DP210101353 and IH210100048. The presented numerical computations are undertaken with the assistance of resources and services from the National Computational Infrastructure (NCI), which is supported by the Australian Government.

References

[1] Yu Y, Gao W, Castel A, Chen X, Liu A. An integrated framework for modelling time-dependent corrosion propagation in offshore concrete structures. Eng Struct 2021; 228:111482.
[2] Sun Bo, Xiao R-C, Ruan W-D, Wang P-b. Corrosion-induced cracking fragility of RC bridge with improved concrete carbonation and steel reinforcement corrosion models. Eng Struct 2020;208:110313.
[3] Wang YZ, Zhao YX, Gong FY, Dong JF, Maekawa K. Developing a three-dimensional finite element analysis approach to simulate corrosion-induced concrete cracking in reinforced concrete beams. Eng Struct 2022;257:114072.
[4] Chen S, Duffield C, Miramini S, Nasim Khan Raja B, Zhang L. Life-cycle modelling of concrete cracking and reinforcement corrosion in concrete bridges: A case study. Eng Struct 2021;237:112143.
[5] Hájková K, Šmilauer V, Jendele L, Červenka J. Prediction of reinforcement corrosion due to chloride ingress and its effects on serviceability. Eng Struct 2018; 174:768–77.
[6] Michel A, Otieno M, Stang H, Geiker MR. Propagation of steel corrosion in concrete: Experimental and numerical investigations. Cem Concr Compos 2016;70: 171–82.
[7] Yu Y, Chen X, Gao W, Wu D, Castel A. Impact of atmospheric marine environment on cementitious materials. Corros Sci 2019;148:366–78.
[8] Yu Y, Gao W, Castel A, Liu A, Feng Y, Chen X, et al. Modelling steel corrosion under concrete non-uniformity and structural defects. Cem Concr Res 2020;135:106109.
[9] Hong S, Zheng F, Shi G, Li J, Luo X, Xing F, et al. Determination of impressed current efficiency during accelerated corrosion of reinforcement. Cem Concr Compos 2020;108:103536.
[10] Wang X, Zhang W, Gu X, Dai H. Determination of residual cross-sectional areas of corroded bars in reinforced concrete structures using easy-to-measure variables. Constr Build Mater 2013;38:846–53.
[11] Zhu W, Dai J-G, Poon C-S. Prediction of the bond strength between non-uniformly corroded steel reinforcement and deteriorated concrete. Constr Build Mater 2018; 187:1267–76.
[12] Almusallam AA. Effect of degree of corrosion on the properties of reinforcing steel bars. Constr Build Mater 2001;15(8):361–8.
[13] Sola E, Ožbolt J, Balabanić G, Mir ZM. Experimental and numerical study of accelerated corrosion of steel reinforcement in concrete: Transport of corrosion products. Cem Concr Res 2019;120:119–31.
[14] Otieno M, Beushausen H, Alexander M. Chloride-induced corrosion of steel in cracked concrete–Part I: Experimental studies under accelerated and natural marine environments. Cem Concr Res 2016;79:373–85.
[15] Yu Q-Q, Gu X-L, Zeng Y-H, Zhang W-P. Flexural behavior of Corrosion-Damaged prestressed concrete beams. Eng Struct 2022;272:114985.
[16] Elghazy M, El Refai A, Ebead U, Nanni A. Experimental results and modelling of corrosion-damaged concrete beams strengthened with externally-bonded composites. Eng Struct 2018;172:172–86.
[17] Koleva DA, Copuroglu O, van Breugel K, Ye G, de Wit JHW. Electrical resistivity and microstructural properties of concrete materials in conditions of current flow. Cem Concr Compos 2008;30(8):731–44.
[18] Bahekar PV, Gadve SS. Impressed current cathodic protection of rebar in concrete using Carbon FRP laminate. Constr Build Mater 2017;156:242–51.
[19] Li W-Q, Pei C, Zhu Y, Zhu J-H. Effect of chopped carbon fiber on interfacial behaviors of ICCP-SS system. Constr Build Mater 2021;275:122117.
[20] García J, Almeraya F, Barrios C, Gaona C, Núñez R, López I, et al. Effect of cathodic protection on steel–concrete bond strength using ion migration measurements. Cem Concr Compos 2012;34(2):242–7.
[21] Lu Y-y, Hu J-y, Li S, Tang W-s. Active and passive protection of steel reinforcement in concrete column using carbon fibre reinforced polymer against corrosion. Electrochim Acta 2018;278:124–36.
[22] Guo W, Hu J, Ma Y, Huang H, Yin S, Wei J, et al. The application of novel lightweight functional aggregates on the mitigation of acidification damage in the external anode mortar during cathodic protection for reinforced concrete. Corros Sci 2020;165:108366.
[23] Feng R, Wang J, Zhu J-H, Dong Z. Fatigue behavior of corroded reinforced concrete continuous beams with multi-intervention system. Eng Struct 2021;231:111748.

[24] Wei L, Zhu J-H, Ueda T, Matsumoto K. Performance of FRCM composites and FRCM-strengthened RC beams subjected to anodic polarization and cyclic loading. Eng Struct 2022;250:113475.
[25] Wilson K, Jawed M, Ngala V. The selection and use of cathodic protection systems for the repair of reinforced concrete structures. Constr Build Mater 2013;39:19–25.
[26] Guo B, Qiao G, Han P, Fu Q. Numerical study on effects of the degree of water saturation on ICCP of chloride-contaminated RC structures. J Build Eng 2022;45:103619.
[27] Guo B, Qiao G, Li Z, Li D, Dai J, Wang Y. Impressed current cathodic protection of chloride-contaminated RC structures with cracking: A numerical study. Journal of Building Engineering 2021;44:102943.
[28] Qiao G, Guo B, Ou J, Xu F, Li Z. Numerical optimization of an impressed current cathodic protection system for reinforced concrete structures. Constr Build Mater 2016;119:260–7.
[29] Fu C, Jin N, Ye H, Liu J, Jin X. Non-uniform corrosion of steel in mortar induced by impressed current method: An experimental and numerical investigation. Constr Build Mater 2018;183:429–38.
[30] Chen J, Fu C, Ye H, Jin X. Corrosion of steel embedded in mortar and concrete under different electrolytic accelerated corrosion methods. Constr Build Mater 2020;241:117971.
[31] Kranc SC, Sagüés AA. Detailed modeling of corrosion macrocells on steel reinforcing in concrete. Corros Sci 2001;43(7):1355–72.
[32] Yu Y, Dong B, Gao W, Sofi A. Physics-based stochastic aging corrosion analysis assisted by machine learning. Probab Eng Mech 2022;69:103270.
[33] Meng Z, Liu Q-F, Xia J, Cai Y, Zhu X, Zhou Yu, et al. Mechanical–transport–chemical modeling of electrochemical repair methods for corrosion-induced cracking in marine concrete. Comput -Aided Civ Infrastruct Eng 2022;37(14):1854–74.
[34] Oldham K, Myland J. Fundamentals of electrochemical science. Elsevier; 2012.
[35] Xia J, Li T, Fang JX, Wl J. Numerical simulation of steel corrosion in chloride contaminated concrete. Constr Build Mater 2019;228:116745 -.
[36] Attarchi M, Brenna A, Ormellese M. FEM simulation of corrosion under macro-cell mechanism. Corros Sci 2021;179:109116 -.
[37] Yu Y, Gao W, Feng Y, Castel A, Chen X, Liu A. On the competitive antagonism effect in combined chloride-sulfate attack: A numerical exploration. Cem Concr Res 2021;144:106406 -.
[38] Chen J, Zhang W, Gu X. Modeling time-dependent circumferential non-uniform corrosion of steel bars in concrete considering corrosion-induced cracking effects. Eng Struct 2019;201:109766.
[39] Hornbostel K, Larsen CK, Geiker MR. Relationship between concrete resistivity and corrosion rate - A literature review. Cem Concr Compos 2013;39:60–72.
[40] Garcia D, Laurens S, Panin S. A comprehensive study of the spatial distribution of the galvanic protection current supplied by zinc layer anodes applied to steel-reinforced concrete structures. Corros Sci 2019;158:108108 -.
[41] Yu Y, Chen X, Gao W, Wu D, Castel A. Modelling non-isothermal chloride ingress in unsaturated cement-based materials. Constr Build Mater 2019;217:441–55.
[42] Zienkiewicz OC, Taylor RL, Nithiarasu P, Zhu JZ. The finite element method. McGraw-hill London; 1977.
[43] Cao Z, Fei Q, Jiang D, Kapania RK, Wu S, Jin H. A sensitivity-based nonlinear finite element model updating method for nonlinear engineering structures. Appl Math Model 2021;100:632–55.
[44] Deng F, Yu W, Liang X, Shen S. A mixed finite element method for large deformation of flexoelectric materials. Appl Math Model 2023;118:303–21.
[45] Dong B, Yu Y, Gao W, Zhao G. A novel method for chloride-induced corrosion analysis incorporating consistent ionic diffusivity and concrete resistivity. Constr Build Mater 2023;365:129941.
[46] Hussain RR, Ishida T. Enhanced electro-chemical corrosion model for reinforced concrete under severe coupled action of chloride and temperature. Constr Build Mater 2011;25(3):1305–15.
[47] Wang Z, Maekawa K, Takeda H, Gong F. Numerical simulation and experiment on the coupled effects of macro-cell corrosion and multi-ion equilibrium with pseudo structural concrete. Cem Concr Compos 2021;123:104181 -.
[48] Guo B, Qiao G, Li D, Ou J. Multi-species reactive transport modeling of electrochemical corrosion control in saturated concrete structures including electrode reactions and thermodynamic equilibrium. Constr Build Mater 2021;278:122228 -.
[49] Cheng X, Su Q, Ma F, Liu X, Liang X. Investigation on crack propagation of concrete cover induced by non-uniform corrosion of multiple rebars. Eng Fract Mech 2018;201:366–84.
[50] Zhao Y, Ren H, Dai H, Jin W. Composition and expansion coefficient of rust based on X-ray diffraction and thermal analysis. Corros Sci 2011;53(5):1646–58.
[51] Jiang B, Doi K, Tsuchiya K, Kawano Y, Kori A, Ikushima K. Micromechanical properties of steel corrosion products in concrete studied by nano-indentation technique. Corros Sci 2020;163:108304.
[52] Dong H, Du X, Han Q, Bi K, Hao H. Hysteretic performance of RC double-column bridge piers with self-centering buckling-restrained braces. Bull Earthquake Eng 2019;17(6):3255–81.
[53] Goyal A. Zinc-Based Anodes for Cathodic Protection of Reinforced Concrete Structures. In: Gupta AK, Shukla SK, Azamathulla H, editors. Advances in Construction Materials and Sustainable Environment. Singapore: Springer Singapore; 2022. p. 45–52.
[54] Protecting Reinforced Concrete Structures with External Zinc Anodes. https://www.materialsperformance.com/articles/coating-linings/2020/11/protecting-reinforced-concrete-structures-with-external-zinc-anodes, 2022 (accessed 29 November 2022).
[55] Tian Z, Ye H. Mechanisms underlying the relationship between electrical resistivity and corrosion rate of steel in mortars. Cem Concr Res 2022;159:106867.
[56] Depoe Bay Bridge. https://mapio.net/pic/p-15620104/, 2022 (accessed 29 November 2022).
[57] Zhang G, Tian Ye, Jin X, Zeng Q, Jin N, Yan D, et al. A self-balanced electrochemical model for corrosion of reinforcing steel bar in considering the micro-environments in concrete. Constr Build Mater 2020;254:119116.
[58] Pedeferri P. Cathodic protection and cathodic prevention. Constr Build Mater 1996;10(5):391–402.
[59] Bertolini L, Redaelli E. Throwing power of cathodic prevention applied by means of sacrificial anodes to partially submerged marine reinforced concrete piles: Results of numerical simulations. Corros Sci 2009;51(9):2218–30.
[60] Liu T, Weyers RW. Modeling the dynamic corrosion process in chloride contaminated concrete structures. Cem Concr Res 1998;28(3):365–79.
[61] Hassanein AM, Glass GK, Buenfeld NR. Protection current distribution in reinforced concrete cathodic protection systems. Cem Concr Compos 2002;24(1):159–67.